

---

# DRAFT CMS Paper

*The content of this note is intended for CMS internal use and distribution only*

---

2009/08/20

Archive Id: 1.37

Archive Date: 2009/08/20 08:54:54

## Crystal ECAL Performance and Operation

The CMS Collaboration

### Abstract

This paper describes the operation and general performance of the CMS Crystal Electromagnetic Calorimeter (ECAL) during cosmic ray tests following the closure of the CMS detector in late 2008. The overall status of the 75 848 channels corresponding to the ECAL Barrel and Endcap detectors is described, and the stability of the ECAL high voltage, temperature, electronic noise, and light monitoring systems is summarised.

This box is only visible in draft mode. Please make sure the values below make sense.

PDFAuthor: The CMS Collaboration  
PDFTitle: Crystal ECAL Performance and Operation  
PDFSubject: CMS  
PDFKeywords: CMS, physics, hardware

Please also verify that the abstract does not use any user defined symbols.



## 1 Introduction

A detailed description of the Compact Muon Solenoid (CMS) experiment at the CERN LHC can be found elsewhere [1]. The central feature of the CMS apparatus is a superconducting solenoid, of 6 m internal diameter. Within the field volume are the silicon pixel and strip tracker, the crystal electromagnetic calorimeter (ECAL) and the brass-scintillator hadronic calorimeter (HCAL). Muons are measured in gas chambers embedded in the iron return yoke. Besides the barrel and endcap detectors, CMS has extensive forward calorimetry.

The CMS ECAL is a fine grained hermetic calorimeter consisting of 75 848 lead tungstate ( $\text{PbWO}_4$ ) crystals, which provide fast response, radiation resistance and excellent energy resolution. The detector consists of a barrel region, constructed from 36 individual supermodules, extending to a pseudorapidity  $\eta$  of 1.48, and two endcaps, which provide coverage to  $\eta = 3.0$ . Scintillation light from the crystals is detected by Avalanche Photodiodes (APDs) in the barrel region and by Vacuum Phototriodes (VPTs) in the endcaps.

In order to achieve the desired energy resolution of ECAL, it is necessary to maintain the stability of the detector calibration over time. This places stringent requirements on the stability of the temperature of ECAL and of the applied high voltage to the APDs. This is due to the temperature dependence of the crystal light yield, as well as the sensitivity of the photodetector gains to variations in both temperature and high voltage. In addition, changes in crystal transparency under irradiation must also be tracked and corrected for.

This paper describes the performance of ECAL during cosmic ray tests in 2008. These tests were the first opportunity to exercise the entire barrel and endcap calorimeter as installed within CMS over an extended period of time. During October and November 2008, the full CMS detector, with the exception of the Preshower detectors, was operated with the magnetic field at 3.8 T for the first time. This paper will summarise the data taken by ECAL over this period and present the achieved stability of temperature, high voltage and electronics noise. Progress in validating the light monitoring system and verifying the pre-existing calibration constants is also presented.

## 2 ECAL in CMS

The 36 supermodules in the ECAL barrel (EB) each consist of 1700 tapered  $\text{PbWO}_4$  crystals with a rear area of  $2.6 \times 2.6 \text{ cm}^2$  and a length of 23 cm (corresponding to 25.8 radiation lengths). The crystal axes are inclined at an angle of  $3^\circ$  relative to the interaction point, in both the  $\phi$  and  $\eta$  projections. Scintillation light from the crystals (approximately 4.5 photoelectrons/MeV at  $18^\circ\text{C}$ ) is detected by two Hamamatsu S8148  $5 \times 5 \text{ mm}^2$  APDs, which were specially developed for CMS and operate at a gain of 50. These are connected in parallel to the on-detector readout electronics, which are organised in units of  $5 \times 5$  crystals corresponding to a trigger tower. Each trigger tower consists of five Very Front End (VFE) cards, each of which accept data from 5 APD pairs. The APD signals are pre-amplified and shaped by Multiple Gain Pre-Amplifier (MGPA) ASICs located on the VFE boards, which consist of three parallel amplification stages (1,6 and 12) [2]. The output is digitised by a 12-bit ADC running at 40 MHz, which selects the gain with the highest non-saturated signal. The data from five VFE cards is transferred to a single front-end card, which generates the trigger primitive data [3], and transmits it to the dedicated off-detector trigger electronics.

The two ECAL endcaps (EE) are constructed from four half-disk Dees, each consisting of 3662 tapered crystals, with a rear area of  $3 \times 3 \text{ cm}^2$  and a length of 22 cm, arranged in a quasi-

projective geometry. The crystals are focussed at a point 1.3 m upstream of the nominal interaction point, with off-pointing angles between  $2^\circ$  and  $8^\circ$ . The crystals in each Dee are organised into 138 standard  $5 \times 5$  supercrystal units, and 18 special supercrystals that are located at the inner and outer radii. Scintillation light is detected by type PMT188 VPTs produced by NRIE with an active area of  $280 \text{ mm}^2$  and operating at gains of 8–10, which are glued to the rear face of the crystals. The VPTs installed in CMS have a 25% (RMS) range of yields and were sorted into six batches across the detector. The highest yield VPTs are installed along the outer circumference of the endcap and the lowest yield tubes are installed along the inner circumference, ensuring a roughly constant transverse energy equivalent of the noise as a function of  $\eta$ . Further details of the design and construction of ECAL, the associated on-detector and off-detector readout electronics and the performance of individual system components can be found elsewhere [1].

Installation of the ECAL barrel into CMS was performed during 2007, with the final module installed in July of that year. Prior to this, all supermodules were fully tested in the laboratory after construction and were exposed to cosmic rays for a period of ten days to obtain relative channel-to-channel inter-calibration constants. Nine of the 36 supermodules were also exposed to test beam electrons to provide absolute energy calibrations (described further in Section 5). During 2006, two supermodules were installed and tested in CMS on the surface at 4 T along with other sub-detectors [4]. The endcap Dees were constructed and commissioned at CERN during early 2008. The Dees were installed in CMS during July 2008 and the entire barrel and endcap calorimeter was commissioned prior to the closure of CMS in late August in preparation for first LHC beam. The silicon preshower detectors, which are located in front of the ECAL endcap were not included in CMS for the 2008 run. They were installed during early 2009 and will be fully commissioned prior to LHC operation in late 2009.

During 2008, a programme of cosmic muon data taking was carried out, prior to first beam from LHC in September 2008. Four runs of approximately two to four week duration, were taken at 0 T; the first three included the ECAL barrel and the fourth run included both the barrel and endcap. Following the suspension of beam operations in mid-September, the CMS Collaboration conducted a month-long data taking exercise known as the Cosmic Run At Four Tesla (CRAFT) during October–November 2008, with the goal of commissioning the experiment for an extended operating period [5]. With all installed detector systems participating, CMS recorded 270 million cosmic ray triggered events with the solenoid at its nominal axial magnetic field strength of 3.8 T. Both the ECAL barrel and endcap participated in CRAFT. One or both endcaps were occasionally removed from global data taking and used to make measurements of the VPT behaviour in the presence of the CMS magnetic field, and to study the effect of pulsing rate on VPT stability (discussed in Section 6).

### 3 General Performance

Of the 270 million cosmic events recorded at 3.8 T, a total of 246 million were used in ECAL reconstruction and analysis. Of these, 158 million events were taken with the nominal APD gain of 50 (G50), in order to study trigger performance, noise and the signatures of minimum ionising particles (MIP) in the configuration that will be used for collision data. In order to study cosmic ray muon signatures in ECAL with greater efficiency, the remaining 88 million events were taken with APD gain 200 (G200) - which is a factor of four higher than the nominal gain for collision data - in order to obtain a higher signal to noise ratio for the MIP signals. For these two gains, the approximate ADC to MeV conversion factors in EB are  $1 \text{ ADC} \approx 37(8.75) \text{ MeV}$  for G50 and G200 respectively.

91 The ECAL trigger was operated in the barrel region during CRAFT, using data taken with APD  
 92 G50. The trigger algorithm used in CRAFT, which is described in detail in [3], involves the gener-  
 93 eration of trigger primitive data for each trigger tower. These provide a measurement of the  
 94 total transverse energy ( $E_T$ ) of the trigger tower, as well as a single (fine-grain) bit that indicates  
 95 the transverse extent of the energy deposit. In CRAFT, a threshold (in  $E_T$ ) of 750 MeV was ap-  
 96 plied at the trigger tower level. These trigger primitives were sent to the Regional Calorimeter  
 97 Trigger (RCT) [6]. Electromagnetic candidates were formed by requiring that the summed  $E_T$   
 98 in two neighboring towers exceeds a threshold of 1 GeV, the fine-grain bit was set (indicating  
 99 a compact lateral extent of the energy deposition), and that the associated energy deposition in  
 100 the hadronic calorimeter was low relative to the energy deposited in ECAL<sup>1</sup>. The typical trig-  
 101 ger rate during CRAFT after applying this algorithm on cosmic events was 30–40 Hz. Further  
 102 details can be found in the paper on Level-1 Trigger performance in this volume [6].

103 In EB, a selective readout algorithm [8] was applied to reduce the ECAL raw data to the level  
 104 of 100 kB/event, which is the bandwidth allocated to the calorimeter readout by the CMS DAQ  
 105 system, with minimal impact on energy resolution and linearity performance. For a particular  
 106 event, the trigger towers were classified as low or high interest, based on their measured  $E_T$ .  
 107 For high interest towers, all channels within a  $3 \times 3$  trigger tower matrix, centred on the seed  
 108 tower, were read out. For low interest towers, only channels with amplitudes above a minimum  
 109 threshold, termed the zero suppression (ZS) threshold, were read out. During CRAFT, towers  
 110 in EB with  $E_T$  greater than 687.5 MeV (APD G50) were classified as high interest. The zero  
 111 suppression threshold was 2.25 ADC counts (approximately 90 MeV in G50), corresponding  
 112 to approximately twice the measured noise level in MGPA gain 12. In EE, a zero suppression  
 113 threshold of 3.0 ADC counts (1.5 times the noise level in gain 12) was applied to all channels.

114 The first step in the analysis of cosmic data in ECAL is the reconstruction of the signal ampli-  
 115 tude and time for each crystal. A fit was performed to the 10 individual digitised 25 ns time  
 116 samples in order to estimate the signal amplitude and timing, using a parameterised pulse  
 117 shape function, with fixed shape parameters optimised separately for barrel and endcap crys-  
 118 tals. The baseline pedestal value was estimated from the first three digitized samples. This  
 119 pulse amplitude and time reconstruction method was used for cosmic muon events that are  
 120 asynchronous with respect to the 40 MHz sampling frequency of the ADC. For LHC beam run-  
 121 ning, where the readout samples are synchronised to the 40 MHz LHC frequency, the standard  
 122 amplitude reconstruction method is a digital filtering technique [9]. This method estimates  
 123 the pulse amplitude by a linear weighting of the individual samples, where the position of  
 124 the pulse maximum is exactly known. Further details of the ECAL time reconstruction perfor-  
 125 mance during CRAFT are described elsewhere in this volume [10].

126 These reconstructed hits were then grouped into clusters of  $5 \times 5$  crystals. The clusters are  
 127 seeded from a single crystal with a reconstructed amplitude greater than 15 ADC counts above  
 128 pedestal (corresponding to 120 MeV for APD G200 or 12.5 standard deviations above pedestal  
 129 in MGPA gain 12), or from two adjacent crystals with amplitudes greater than 5 ADC (approx-  
 130 imately 40 MeV in G200) above pedestal. Adjacent clusters in  $\phi$  were grouped together to form  
 131 superclusters. In APD G200, the probability for a muon traversing the length of a crystal in  
 132 the ECAL Barrel to produce a reconstructed cluster is greater than 99% [11]. For muons that  
 133 cross the tracker volume, which are used in the  $dE/dx$  analysis described in section 5.1 and  
 134 should pass through ECAL twice, there are an average of 1.67 reconstructed superclusters per  
 135 event. This reduction is due to some muons either passing through non-operating regions of  
 136 the barrel (supermodules with low voltage turned off) or passing through the forward regions

<sup>1</sup>A much higher threshold on the  $E_T$  of electromagnetic candidates will be applied for LHC beam running. For a luminosity of  $2 \times 10^{33} \text{ cm}^{-2}\text{s}^{-1}$ , a threshold of 26 GeV is envisaged for single electron/photon candidates [7].

137 of the detector.

138 The fraction of channels that were operational during CRAFT was 98.33% in EB (60177/61200)  
 139 and 99.66% in EE (14598/14648). For the barrel, power to 28/2448 trigger towers (1.14%) was  
 140 cut due to a damaged LV supply cable, which was repaired after CRAFT. The readout from a  
 141 total of 11 trigger towers (0.45%) was suppressed in the barrel readout due to data integrity  
 142 problems. A total of 48 channels (0.08%) were classified as inoperable - based on problems ob-  
 143 served in pedestal data and low response to injected laser light and beam-induced muon data  
 144 from the September 2008 LHC beam tests. An additional 35 single channels were classified as  
 145 problematic, but could be operated in at least one of the three MGPA gains. These 83 (48 inop-  
 146 erable plus 35 problematic) channels were masked in the ECAL cosmic reconstruction. Most of  
 147 them have been known since detector commissioning, with 16 new channels discovered since  
 148 installation in CMS. For the endcap, data from two supercrystals, corresponding to 50/14648  
 149 channels (0.34%) were suppressed due to a broken data optical fibre inside the Dee (25 chan-  
 150 nels) and a faulty low voltage connection powering five VFEs (25 channels). No isolated dead  
 151 channels were observed in the endcap data.

## 152 4 System stability

153 The excellent energy resolution offered by the fine grained electromagnetic calorimeter of CMS  
 154 depends on precise control of temperature and high voltage, minimising the rate of electronics  
 155 noise and accurately measuring and correcting for changes in crystal light yield caused by  
 156 radiation damage.

157 The EM energy resolution can be parameterised as a function of the incident electron/photon  
 158 energy,  $E$  (in GeV), as follows:

$$\frac{\sigma_E}{E} = \frac{a}{\sqrt{E}} \oplus \frac{b}{E} \oplus c \quad (1)$$

159 where  $a$  represents the stochastic term, which depends on event-by-event fluctuations in lateral  
 160 shower containment, photostatistics and photodetector gain;  $b$  represents the noise term, which  
 161 depends on the level of electronics noise and event pile-up;  $c$  represents the constant term,  
 162 which depends on non-uniformity of the longitudinal light collection, leakage of energy from  
 163 the rear face of the crystal and the accuracy of the detector inter-calibration constants. The  
 164 target value for the constant term is 0.5% for both the barrel and endcap [12].

165 Previous measurements taken with test beam electrons with energies between 20 and 250 GeV  
 166 have shown that the energy resolution and noise performance of the ECAL barrel meets the  
 167 design goals for the detector [13]. The following sections describe the achieved stability of  
 168 electronics noise, temperature, gain, and the ECAL light monitoring system for data taken  
 169 during 2008.

### 170 4.1 Noise stability

171 The electronics noise of ECAL was monitored during CRAFT from dedicated pedestal runs  
 172 (which measure the noise in all three gains of the MGPA) and during cosmic muon running for  
 173 MGPA gain 12 (by analysing the three pre-samples of each ten sample data frame). Figures 1(a)  
 174 and (b) show the stability of the per-channel noise level (expressed in ADC counts) in EB and  
 175 EE for MGPA gain 12 using pedestal runs recorded during CRAFT. For barrel data, the signal  
 176 amplitude was reconstructed for each event making use of a digital filtering technique using

177 five consecutive digitized samples around the expected position of the peak. As stated above,  
178 this is the baseline method for clock-synchronous LHC running [9]. The pedestal was dynam-  
179 ically subtracted from each event using three pre-samples before the peak. This “3+5 weight”  
180 method is known to be effective in reducing the level of low frequency (or pickup) noise [9].  
181 The noise level for the barrel was defined as the RMS deviation of the reconstructed signal am-  
182 plitude measured from each pedestal event. For the endcap, the noise level was defined as the  
183 RMS deviation of the three pre-samples, summed over all pedestal events.

184 The data shown in Figure 1(a) were taken with both APD G50 and G200 in the barrel, and  
185 with the CMS magnetic field at 0 T and 3.8 T. For MGPA gain 12, the average noise level per  
186 channel was 1.06 ADC counts in the barrel, and 1.96 ADC counts in the endcap. The noise level  
187 in ECAL does not depend on the CMS magnetic field or the Barrel APD gain. The observed  
188 noise levels in EB and EE in CMS are also consistent with the values measured during module  
189 construction (see, for example, Table 1 of [9] for EB noise measurements obtained with test  
190 beam data), and meet the MPGA design specifications [2]. For the barrel, the average value of  
191 the noise in energy equivalent units corresponds to roughly 40 MeV/channel (APD G50). The  
192 per-channel noise stability during CRAFT is shown in Figure 1(b). This shows the variation  
193 (RMS) of the noise level measured in MGPA gain 12 plotted for each individual channel, and  
194 computed over the pedestal runs used in Figure 1(a). The average per-channel variation was  
195 0.127 ADC counts in the barrel and 0.161 ADC counts in the endcaps. The performance of the  
196 MGPA was also shown to be insensitive to the CMS magnetic field at the per-mille level using  
197 dedicated charge injection runs.

198 A small number ( $< 0.1\%$ ) of single channels showed high noise levels during CRAFT (either  
199 high pedestal RMS - greater than 2.0 ADC counts in the barrel, and 3.0 ADC counts in the  
200 endcaps, or high occupancy in cosmic muon runs). These channels were excluded in the subse-  
201 quent reprocessing of the CRAFT data. An additional noise contribution was observed in 9 of  
202 the 36 barrel supermodules during CRAFT from an analysis of the fluctuation of the ten sam-  
203 ples in each pedestal event. In these supermodules, the average single sample noise in MGPA  
204 gain 12 was  $\approx 1.25$  ADC counts, compared to 1.1 ADC counts for the other supermodules.  
205 This is believed to be low frequency ( $< 4$  MHz) pickup noise associated with the operation of  
206 other CMS subdetectors in the underground cavern. However, this noise is not observed in  
207 the amplitudes reconstructed by the digital filter technique - the noise level and noise stability  
208 shown in Figures 1(a) and (b) are uniform across all barrel supermodules. No significant source  
209 of additional noise was observed in either of the endcap detectors.

## 210 4.2 High Voltage stability

211 High Voltage is supplied to the barrel APDs via a custom HV power supply developed in  
212 collaboration with CAEN. A total of 18 CAEN SY1527 crates are used. These are located in the  
213 CMS service cavern at a distance of 120m from ECAL, and sense wires are used to correct for  
214 voltage drops in the HV supply lines between the crates and the detector. Each crate contains 8  
215 A1520E boards, which carry up to 9 channels. Each channel can give a bias voltage of 0–500 V  
216 to 50 APD pairs (maximum current 15 mA). A total of 1224 HV channels are used in the ECAL  
217 barrel. The APDs are sorted according to operating voltage, and paired such that the mean  
218 gain is 50. The nominal operating voltage is between 340 and 430 V. Since the APD gain,  $M$ , is  
219 very sensitive to the bias voltage ( $1/M(\partial M/\partial V) \approx 3\%/V$ ), the operating voltage must be kept  
220 stable to several tens of mV. The HV crates are fully integrated into the CMS Detector Control  
221 System (DCS) framework which allows remote control and monitoring of the applied voltages  
222 and currents for each channel. High Voltage is supplied to the endcap VPTs by two CAEN  
223 SY1527 crates, one for each endcap. The cathodes are at ground potential, the dynodes are held

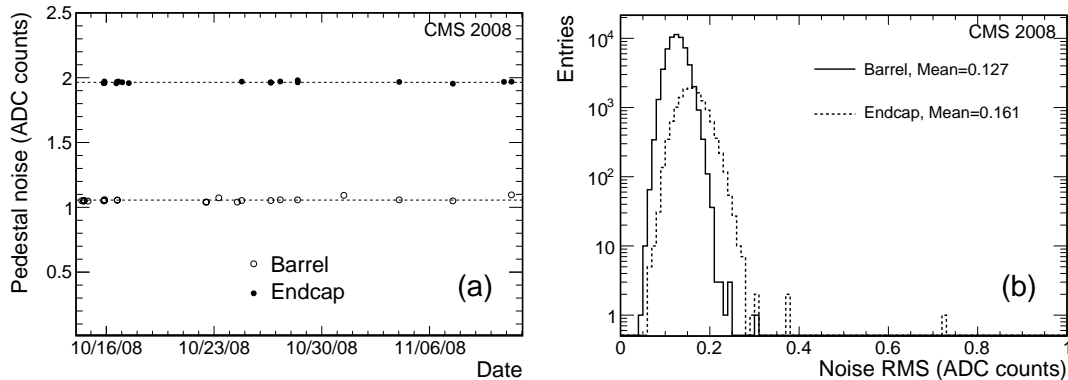


Figure 1: Pedestal noise stability during CRAFT. (a) Average per-channel electronic noise in the barrel and endcaps versus time for pedestal data taken during CRAFT. Data in MGPA gain 12 is used, and the noise level is expressed in ADC counts. The dashed lines represent the average noise levels in the barrel and endcaps respectively; (b) Distribution of the RMS of the pedestal noise for each channel, calculated from the pedestal runs shown in (a).

224 at 600 V and the anodes at 800 V. Four pairs (anode and dynode) of CAEN channels are used at  
 225 each end, so each pair supplies approximately one quadrant. In addition, there is an interlock  
 226 on the CAEN boards, to switch off the high voltage to the VPTs if the CMS magnetic field is not  
 227 at a constant value.

228 During the CRAFT data taking period HV was supplied to the barrel APDs with two different  
 229 settings, corresponding to G50 and G200 respectively. A one-week period during CRAFT has  
 230 been identified where all channels were on 24 hours a day, and at APD G50. Figure 2(a) shows  
 231 the monitored voltage on one HV sense wire recorded by the CAEN crate and logged in the  
 232 CMS detector conditions database. All the points are compatible with a constant value within  
 233 the measurement errors. The line is the average over this period. The stability of the sense wire  
 234 readings for the barrel HV channels during this period can be estimated by the distribution  
 235 of the RMS of the readings of each individual channel (Figure 2(b)). The RMS mean value is  
 236 2.1 mV. More than 97% of channels show fluctuations below 5 mV and all are within 10 mV  
 237 during the time period considered here.

238 APD dark current measurements were recorded for each channel by Detector Control Unit  
 239 (DCU) ASICs located on the front-end electronics. The additional voltage drop over the 136 k $\Omega$   
 240 protection resistor between the sense point and the APD cathode could have a sizeable effect  
 241 on the applied voltage for leakage currents of a fraction of a  $\mu$ A. The minimum dark current  
 242 measurable by the DCU system, once the ADC pedestal has been subtracted, is 320 nA. The  
 243 ADC pedestals have been computed averaging several runs taken with no high voltage ap-  
 244 plied to the APDs. The measurements recorded during the CRAFT data taking reported dark  
 245 currents below the measurable threshold for almost all channels in the barrel, as expected for  
 246 non-irradiated APDs, with high currents observed in only 11 channels ( $< 0.02\%$ ).

### 247 4.3 Temperature stability

248 The temperature of the ECAL barrel is required to be stable at the level of 0.05  $^{\circ}$ C. This ensures  
 249 that temperature fluctuations provide a negligible contribution to the constant term of the EM  
 250 energy resolution. Fluctuations in temperature directly affect the light yield of the crystals  
 251 (the temperature coefficient of the light yield is approximately  $-2\%$  per  $^{\circ}$ C) and the gain of the  
 252 APDs in the ECAL Barrel ( $1/M(\partial M/\partial T) \approx -2.3\%$  per  $^{\circ}$ C [14]). In the endcap, the temperature

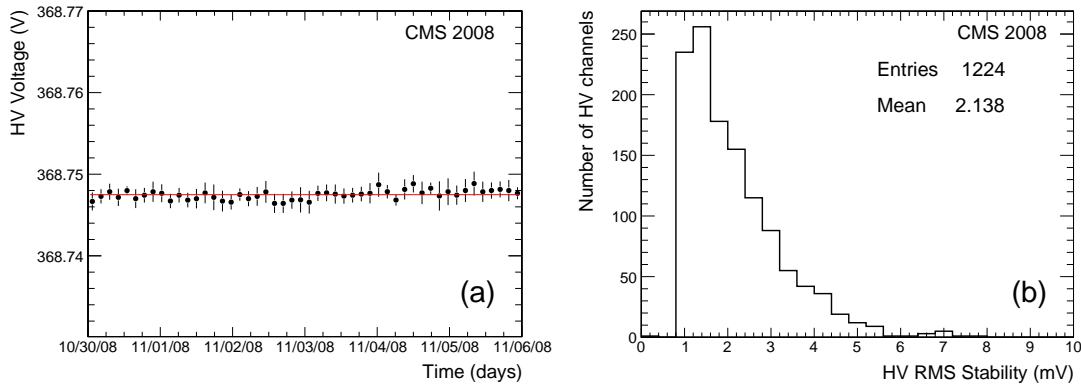


Figure 2: Barrel HV stability during CRAFT. (a) Monitored HV on a barrel sense wire during one week of CRAFT data taking when the APD gain was set to G50. Each data point is averaged over a three hour time period; (b) Distribution of the RMS of the readings for each HV channel during this period.

253 coefficient of the VPT gain is assumed to be negligible relative to the temperature sensitivity of  
 254 the APD gain and crystal light yield [15, 16]. Accordingly, a less stringent temperature stability  
 255 requirement of  $0.1^\circ\text{C}$  is assumed for the endcap Dees.

256 Temperature readings in the barrel are provided by two independent groups of sensors. A  
 257 series of precision temperature monitor (PTM) devices (10 per supermodule, 24 per endcap  
 258 Dee) measure the temperatures on each side of the crystal volume and the temperature of  
 259 the incoming and outgoing cooling water with a relative accuracy of  $\approx 0.01^\circ\text{C}$ . In addition,  
 260 thermistors are fixed to the back of each  $5 \times 2$  crystal matrix (170 per SM) in the barrel and to  
 261 each  $5 \times 5$  crystal matrix in the endcap. These thermistors are read out by DCU ASICs located  
 262 on each VFE board. The thermistors are calibrated in the laboratory prior to installation and  
 263 the response of the DCU ASICs is then calibrated by the PTM devices.

264 Figure 3(a) shows the EB temperature history during CRAFT for three representative PTM sen-  
 265 sors monitoring the temperature close to the rear face of the crystals of three different super-  
 266 modules. An additional sensor monitoring the input cooling water temperature of another  
 267 supermodule is also shown. Each data point is the average of approximately 45 readings  
 268 taken over an eight hour period, and the error bars shown represent the uncertainty on this  
 269 mean value. During CRAFT, these temperature readings were stable to better than  $0.01^\circ\text{C}$ ,  
 270 which is well within the desired stability target. Temperature sensors in both the inner region  
 271 ( $0 < |\eta| < 0.44$ ) of the supermodules, and the outer region ( $1.13 < |\eta| < 1.48$ ) are shown  
 272 (labelled Module 1 and Module 4 respectively). The outer regions of the supermodules are  
 273 observed to be an average of  $0.09^\circ\text{C}$  higher temperature than the inner regions. The mean  
 274 temperature measured in the ECAL barrel during CRAFT was  $18.1 \pm 0.02^\circ\text{C}$  by the PTM sen-  
 275 sors and  $18.12 \pm 0.04^\circ\text{C}$  by the APD capsule thermistors.

276 Figure 3(b) shows the EE temperature history during CRAFT. Three representative PTM sen-  
 277 sors are shown, reading temperatures on the Dee backplates, close to the rear face of the crys-  
 278 tals. An additional sensor monitoring the input cooling water is also shown for reference.  
 279 The readings are shown to be stable at the level of  $\pm 0.02^\circ\text{C}$ , following an initial period of  
 280 temperature stabilization at the beginning of CRAFT. This is again well within the ECAL re-  
 281 quirement for the temperature stability of the endcap detectors. The observed small changes in  
 282 the backplane sensor readings are correlated with fluctuations in the input water temperature.  
 283 The readings in Dee 3 are affected by larger noise fluctuations during much of CRAFT run-

ning relative to the other sensors. These are not related to temperature instability. However, the readings in Dee 3 are observed to follow the same trends versus time as the other sensors shown in the Figure. The mean temperature measured by the PTM sensors in the endcaps during CRAFT was  $18.56 \pm 0.06$  °C.

The RMS deviation of temperature histories was also calculated for the 6009 barrel thermistors and 548 endcap thermistors that were read out during CRAFT. The average stability was 0.0088 °C in the barrel, with all measurements within the ECAL specification of 0.05 °C. The average stability in the endcap was measured to be 0.0166 °C, using data from 15<sup>th</sup> October onwards - once the temperature had stabilised following the initial turn-on period clearly visible in Figure 3(b). Measurements comparing the variation of neighbouring thermistors in the barrel and endcap indicated a higher level of readout noise in the latter. However, even if all of the observed fluctuations in the endcap thermistor readings are attributed to temperature instabilities, practically all of the measurements lie within the specification of 0.1 °C.

#### 4.4 Crystal transparency monitoring

The ECAL laser monitoring (LM) system is critical for maintaining the stability of the constant term of the ECAL energy resolution at high luminosities. Its main purpose is to accurately measure and correct changes in the lead tungstate crystal transparency, which decreases during irradiation at LHC due to formation of colour centres and recovers when there are no collisions, when the colour centres annihilate. The LM system is also able to detect and correct for other effects such as photodetector gain changes due to temperature or high voltage variations.

To reach the ECAL design performance, the LM system is required to monitor transparency changes for each crystal at the 0.2% level, with one measurement every 20–30 minutes. The LM system consists of two different lasers: a blue laser with a wavelength (440 nm) close to the emission peak of scintillation light from PbWO<sub>4</sub>, and an infra-red laser (wavelength 796 nm) for which crystal transparency is stable under irradiation. The blue laser is used to monitor crystal transparency to scintillation light whereas the red laser is used to disentangle effects due to irradiation from other possible effects such as gain variations.

Light is fanned out from the laser sources to the 75 848 crystals by means of a two-level distribution system. A fibre optic switch directs laser pulses via 95–130 m optical fibres to a single calorimeter element located on-detector. There are 72 half-supermodule calorimeter elements in the barrel and 16 quarter-Dee elements in the endcap. The secondary fanout consists of a reflective light splitter, and 9(19) output optical fibres per barrel supermodule (endcap Dee). The tertiary fanout consists of a 12 mm inner-diameter thermoplastic light diffusing sphere with a fanout of typically 200 fibres that carry the laser light to individual crystals. Laboratory measurements indicate a typical light yield spread of 2.4% (RMS) over 240 fibres. For the endcaps, this tertiary light distribution system is shared with a LED pulser system, which was installed in 2008 once the endcap Dees were located in CMS. It contains 76 light sources in two colours: blue (455nm) and orange (617nm). The main purpose of this system is to provide a constant background pulsing rate of > 100 Hz to mitigate the effect of VPT anode sensitivity on rate, as described in Section 6.2. Additional fanout fibres are connected to a set of 528 radiation-hard PN diodes, which provide monitoring of the laser and LED light output, and allow pulse-to-pulse variations in the reconstructed amplitudes to be corrected for.

Changes in the crystal transparency due to radiation damage do not affect the amplitude from the APD signal for an electromagnetic shower (S) in exactly the same way as it affects the signal for injected laser pulses (R), due to different mean path lengths of the light in the crystals. It has been shown that it is possible to relate them simply:  $\frac{S}{S_0} = \left(\frac{R}{R_0}\right)^\alpha$ . This expression, with  $\alpha \approx 1.6$

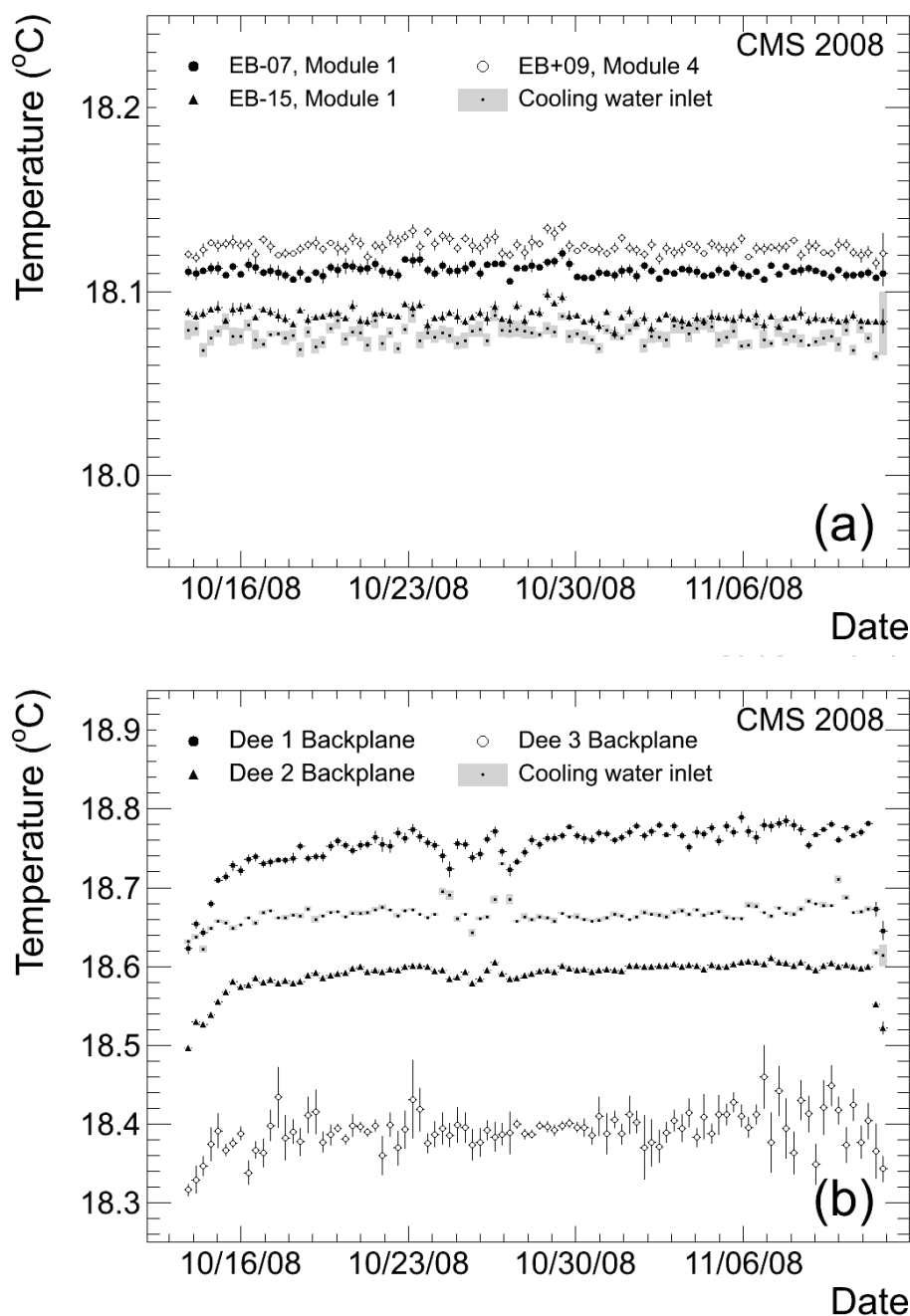


Figure 3: Stability of ECAL temperature measurements during CRAFT: (a) Temperature histories for four representative PTM sensors in the ECAL barrel during CRAFT. The data points show the mean temperature recorded over eight-hour time bins for sensors in four different supermodules. Three of the four sensors monitored the temperature close to the rear face of the crystals, and one sensor recorded the input water temperature in one of the cooling circuits; (b) Temperature histories for four representative PTM sensors in the endcap. Three sensors monitored the temperature on the Dee backplanes, and one monitored the input cooling water temperature. The uncertainties displayed on these plots represent the error on the mean of approximately 45 measurements per data point.

330 was shown to describe well the behaviour of crystals evaluated using test beam data [1, 17].

331 During CRAFT, a total of approximately 500 sequences of laser monitoring data were taken,  
 332 with each sequence injecting 600 laser pulses per crystal. This data was taken within a ‘calibra-  
 333 tion sequence’ of pedestal, MGPA charge injection data and laser data, which was recorded in  
 334 the simulated LHC abort gap during cosmic muon running. The laser typically ran at 100 Hz,  
 335 resulting in laser light injected into  $\mathcal{O}(1\%)$  of the available gaps.

336 In EB, the average over 600 events of the APD to PN response ratio ( $\langle \text{APD}/\text{PN} \rangle$ ) for data taken  
 337 with APD G50 was monitored to track variations of channel response to blue laser light. Due to  
 338 problems reading out the PN diode data during the calibration sequence, two reference APDs  
 339 were instead chosen in each light monitoring region (approx 200 crystals). The reconstructed  
 340 laser amplitudes in the other APDs were normalised relative to these reference channels in  
 341 order to correct for pulse-to-pulse variations in the laser output. Figure 4(a) shows the RMS  
 342 of the quantity  $\langle \text{APD}/\text{APD}_{\text{ref}} \rangle$  for 57300 channels in EB over a 200 hour long period within  
 343 CRAFT when nominal data quality conditions were met<sup>2</sup>. Data from two supermodules (3400  
 344 channels) were excluded from this analysis due to low voltage supply problems during this  
 345 time period. This plot illustrates the performance of the LM system: 99.8% of the monitored  
 346 channels exhibited an  $\langle \text{APD}/\text{APD}_{\text{ref}} \rangle$  stability better than the ECAL requirement of 0.2%. Con-  
 347 sidering all laser data recorded during CRAFT, 98% of the monitored channels satisfied this  
 348 requirement.

349 For EE, the reconstructed laser amplitudes were normalized to a reference VPT in each super-  
 350 crystal. Figure 4(b) shows the RMS of  $\langle \text{VPT}/\text{VPT}_{\text{ref}} \rangle$  over 600 events from the same data taking  
 351 period as shown in Figure 4(a). A total of 13600 endcap channels were monitored. During  
 352 CRAFT the average amplitude from laser light in the endcap crystals was significantly reduced  
 353 from the values expected for nominal data taking (since the end of CRAFT these amplitudes  
 354 have been increased by a factor of 10). As a result, approximately 1000 channels were rejected  
 355 from this analysis, since their laser amplitudes during CRAFT were too low for reliable stability  
 356 measurements. For this data, 98.3% of the monitored endcap channels showed stabilities better  
 357 than 0.2%.

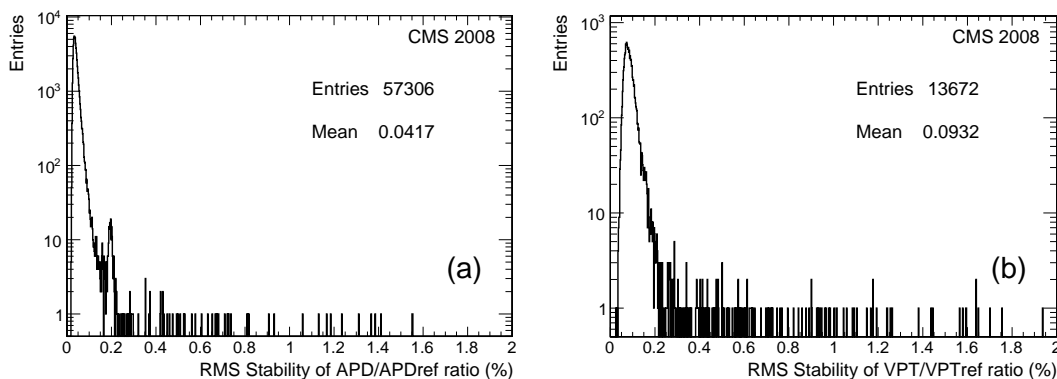


Figure 4: Stability of the ECAL laser monitoring system during CRAFT: (a) RMS deviation of the quantity  $\langle \text{APD}/\text{APD}_{\text{ref}} \rangle$  for EB channels with nominal data quality cuts applied. The origin of the small secondary peak at 0.2%, which arises from six neighbouring trigger towers (150 channels), is under investigation; (b) as (a) but for the quantity  $\langle \text{VPT}/\text{VPT}_{\text{ref}} \rangle$  calculated for EE channels.

<sup>2</sup>In this plot the most stable of the two reference APDs was used in each light monitoring region

## 5 Validation of inter-calibration constants

The precise calibration of ECAL is of crucial importance in maintaining the good energy resolution performance of the device. The channel response uniformity directly impacts the constant term of the EM energy resolution. This uniformity depends on the accuracy of the calibration of the relative response for all channels in the detector. Inter-calibration constants are used to correct for channel-to-channel response variations, for example due to differences in crystal light yield and photodetector gain.

Prior to installation in CMS, 9 of 36 barrel supermodules were calibrated with 90–120 GeV electrons at the H4 test beam at CERN, with an achieved precision of 0.3% [18]. The remaining 27 supermodules were calibrated using cosmic muons, with a precision of 1.5 – 2.5%. For the endcap dees, the pre-calibration constants were determined from laboratory measurements of crystal light yield and VPT gain. A matrix of 460 endcap crystals was inter-calibrated with a precision of better than 1% in an electron test beam during 2007. This data was also used to estimate the precision of the laboratory light yield measurements and VPT gain measurements for a representative subset of 162 crystals. These originate from the manufactured crystal sample that comprises the majority (> 80%) of the installed crystals in CMS, and have the best understood light yield measurements. For these crystals, the combination of light yield and VPT yield measurements were verified with a precision of 7.4% (RMS) by comparing the laboratory and test beam measurements.

The ultimate inter-calibration precision will be obtained from data upon LHC startup. Several data-driven techniques will be used to obtain the inter-calibration constants with an expected precision of  $\approx 0.5\%$  [19]. Data collected in 2008 from cosmic muons and beam-induced muons was used to perform an in situ check of the pre-calibration constants at the level of 1–2% for the barrel and better than 10% in the endcaps. These will provide the initial calibrations for startup LHC physics and the starting values for the beam data-driven calibration methods.

### 5.1 Validation of EB pre-calibration constants

A check of the pre-calibration constants for 14 of the 36 barrel supermodules was performed by comparing the stopping power ( $dE/dx$ ) distributions for cosmic ray muons after the existing constants were applied. Muons with momentum between 5 and 10 GeV/c were used in this analysis. In this momentum region, energy loss by ionization is the dominant process. The muons were required to pass through the tracker volume, and only events taken with APD G200 were used. A total of 250 000 events remained after these cuts.

The momentum selection of the cosmic muons is performed after the muons pass through the upper hemisphere and before they pass through the lower hemisphere of ECAL. This causes a difference in the energy deposits in the two hemispheres of about 0.5%, due to the dependence of  $dE/dx$  on the muon momentum. In order to compare the ECAL response in the upper and lower hemispheres, this effect is corrected for in the analysis. Events were further selected requiring that the angle between the muon trajectory extrapolated from the tracker and the crystal axis is less than  $30^\circ$ . This reduces systematic biases on the energy scale due to crystal energy deposits falling below the clustering or zero suppression thresholds, which is more probable for large angle tracks which pass through multiple crystals [11].

The average response of different supermodules varies by up to 30%, due to differences in crystal light yield. The measured  $dE/dx$  distributions for the 14 supermodules were compared, after first applying the pre-calibration constants to equalise the light yield response. Figure 5(a) shows the mean stopping power for each supermodule, plotted as a function of the

403 average pre-calibration values. Each point is normalised to the average  $dE/dx$  value for all 14  
 404 supermodules. A truncated mean is used, in order to remove statistical fluctuations from high  
 405 energy deposits in the upper 5% of the  $dE/dx$  distributions. The spread of these measurements,  
 406 which indicates the level of uniformity of the detector response, is about 1.1% (RMS). This is  
 407 comparable with the statistical precision of the measurements (typically 0.4%) combined with  
 408 the following systematic uncertainties: a) the dependence of the muon energy scale on the angle  
 409 between the crystal axis and the muon direction (estimated to be 0.5%); b) the variation in  
 410 average muon momentum for different supermodules, since they have different angular accep-  
 411 tance to cosmic rays and hence sample different regions of the cosmic muon flux. This second  
 412 uncertainty is estimated to be 0.4%. The total systematic uncertainty of 0.64% is indicated by  
 413 the shaded band in Figure 5(a).

414 The calibration procedures that utilise LHC data will yield precise inter-calibration of crystals  
 415 at a given  $\eta$  value. The pre-calibration constants will be required to provide the relative scale  
 416 for crystals at different  $\eta$  values at LHC startup. The cosmic muon data taken during CRAFT  
 417 was therefore used to validate in situ the pre-calibration constants as a function of  $\eta$ . Figure 5(b)  
 418 shows the truncated mean  $dE/dx$  as a function of the  $\eta$  index of the ECAL crystals. These mea-  
 419 surements are normalised to the average  $dE/dx$  integrated over all  $\eta$  values. The distribution  
 420 is plotted over the range  $-0.7 < \eta < 0.7$  in which the majority of the muons that pass through  
 421 both the tracker and ECAL are located. The spread of the measurements, indicating the pre-  
 422 cision to which the  $\eta$ -dependent pre-calibration scale is verified, is 0.8% (RMS). The statistical  
 423 precision of the measurements, indicated by the error bars on the points, is typically 0.4%. The  
 424 systematic uncertainty, which is represented by the shaded region, is 0.51%. The main contri-  
 425 bution to the systematic error is the energy scale dependence on the angle between the muon  
 426 trajectory and the crystal axis (0.5%). Since each data point includes contributions from events  
 427 in both the upper and lower hemispheres of ECAL, the systematic uncertainty on the muon  
 428 momentum scale due to the variation in acceptance to the cosmic ray flux is reduced to 0.1% in  
 429 Figure 5(b).

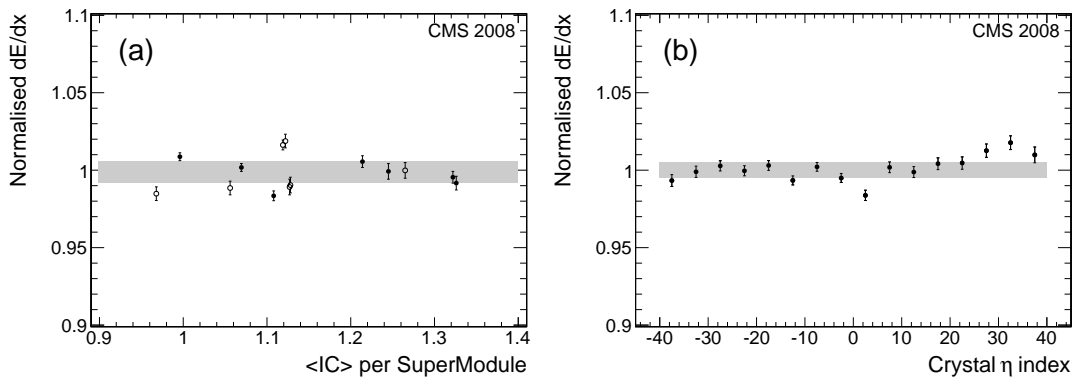


Figure 5: (a) Validation of EB pre-calibration constants using cosmic ray muons. Normalised mean stopping power,  $dE/dx$ , versus mean pre-calibration constants for 14 supermodules. Each point is normalised to the average value for all supermodules. The filled circles indicate supermodules located in the upper hemisphere of ECAL, and the open circles represent supermodules located in the lower hemisphere. (b) Validation of EB inter-ring energy scale. Normalised mean stopping power versus crystal  $\eta$  index. Each data point is integrated over five crystals in  $\eta$  and all values of  $\phi$ . In both plots, the shaded region represents the systematic error on the measurement of  $dE/dx$ .

## 430 5.2 Validation of EE pre-calibration constants

431 A check of the endcap pre-calibration constants was performed using beam-induced muons  
 432 from 41 events recorded by CMS with the magnet at 0 T during LHC beam commissioning.  
 433 The spray of muons produced from the LHC primary beams impinging on collimator blocks  
 434 upstream of the CMS detector produced large (TeV) energy deposits in EB and EE, illuminating  
 435 all active channels. In EE, the average energy per crystal was approximately 5 GeV/event.  
 436 From this energy deposition, a set of local calibration coefficients were first defined, which  
 437 equalise the response over a  $5 \times 5$  crystal matrix:

$$c_{i,local} = \frac{\langle E_i \rangle_{5 \times 5}}{E_i} \quad (2)$$

438

439 where  $E_i$  is the energy deposited in a single crystal, and  $\langle E_i \rangle_{5 \times 5}$  is the average energy  
 440 recorded in the  $5 \times 5$  crystal matrix. Here, it is explicitly assumed that the energy deposition is  
 441 uniform over each  $5 \times 5$  crystal region.

442 Inter-calibration between supercrystals was provided by the pre-calibration constants, which  
 443 account for the radial dependence of the calibration coefficients due to the known variation in  
 444 VPT yield across the endcaps:

$$c_i = c_{i,local} \frac{\langle c_i^{pre} \rangle_{5 \times 5}}{\langle c_{i,local} \rangle_{5 \times 5}} \quad (3)$$

445

446 where  $\langle c_{i,local} \rangle_{5 \times 5}$  and  $\langle c_i^{pre} \rangle_{5 \times 5}$  are the calibration coefficients, averaged over a  $5 \times 5$   
 447 crystal region, from beam-induced muons and laboratory measurements respectively.

448 The inter-calibration constants obtained using this method were compared to those obtained  
 449 from test beam measurements of 460 endcap crystals in Figure 6(a). The difference between the  
 450 normalised coefficients for the two sets of measurements were computed for each crystal. The  
 451 agreement is 10.4% (RMS). The statistical and systematic precision of the constants derived  
 452 from beam-induced muons was investigated. The precision of the constants was evaluated  
 453 with respect to the test beam measurements for an independent set of  $N$  events entering from  
 454 the left and right sides of the detector. The precision was found to require a constant term  
 455 of 8.8%, in addition to the expected  $1/\sqrt{N}$  dependence. This constant term is believed to  
 456 represent the limit of the local uniformity assumption for the energy deposition in the endcaps.

457 Figure 6(b) shows a comparison of test beam and the weighted average of the pre-calibration  
 458 and beam-induced muon coefficients for the reference sample of 162 crystals that were exposed  
 459 to the test beam. By combining the coefficients, an improved agreement from 7.4% (RMS) to  
 460 6.3% (RMS) was observed. This indicates that the coefficients obtained from laboratory and  
 461 beam-induced muon measurements are largely independent. Figure 6(c) shows the compari-  
 462 son of beam-induced muon and pre-calibration constants for 7200 crystals in the positive end-  
 463 cap. Approximately 100 channels were excluded from this plot, due to signal timing problems  
 464 during the beam muon runs, or higher pedestal noise. The RMS of 13.2% is consistent with  
 465 the quadrature sum of the 10.4% uncertainty on the beam-induced muon measurements (Fig-  
 466 ure 6(a)) and the 7.4% uncertainty on the pre-calibration measurements. A similar level of  
 467 agreement was also observed in the negative endcap. With this measurement, it is possible to  
 468 deduce that the 6.3% precision of the combined beam-induced muon and pre-calibration co-  
 469 efficients over the 162 reference crystals that were exposed to the test beam, is valid over all

470 endcap crystals.

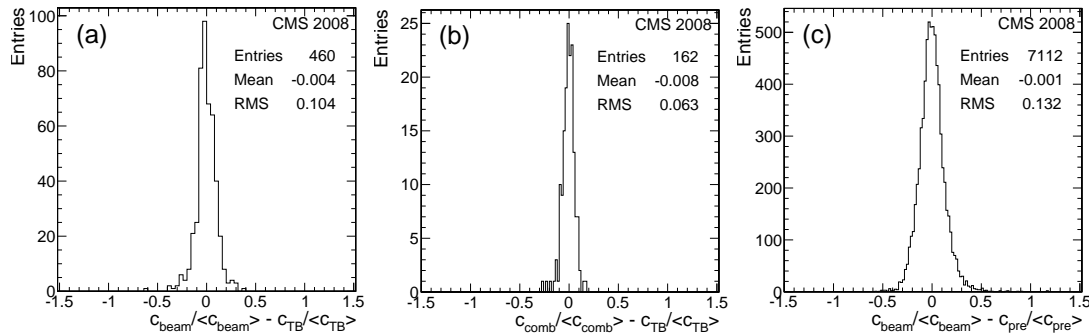


Figure 6: Validation of EE pre-calibration constants using beam-induced muons: (a) comparison between normalised beam-induced muon and test beam coefficients for 460 crystals; (b) comparison of the normalised combined beam-induced muon and pre-calibration coefficients to those derived from test beam data for the sub-sample of 162 production crystals; (c) comparison between normalised beam-induced muon and pre-calibration constants for the entire positive endcap.

## 471 6 VPT performance at 3.8 T

### 472 6.1 VPT yield as a function of angle to magnetic field

473 Laboratory measurements of VPT performance have shown that these devices are able to op-  
 474 erate in the high magnetic field environment of CMS [20]. Measurements taken in CMS during  
 475 2008 with the ECAL laser and LED monitoring systems have permitted the performance of  
 476 the 14 648 installed VPTs to be studied at an operating field of 3.8 T. As well as confirming the  
 477 operability of these devices at high field, these measurements have also allowed the effect of  
 478 magnetic field on the VPT gain to be measured. Over the range of angles subtended by the end-  
 479 cap VPTs to the magnetic field (4 to 18 degrees), the VPT anode response changes by between  
 480 5 and 30% due to this effect. Since the pre-calibration constants for the endcap discussed in the  
 481 previous section, as well as the energy scale derived from test beam measurements, were all  
 482 obtained at zero magnetic field, it is important to account for this field-induced effect in order  
 483 to translate these constants to 3.8 T.

484 A schematic representation of the disposition of the electrode structure of a VPT in a magnetic  
 485 field is shown in Figure 7(a). The response varies as a function of the angle,  $\theta$ , between the  
 486 axis of the device and the magnetic field, and as a function of the orientation,  $\phi$  of the device  
 487 about its axis. The response curve exhibits two main features: a plateau, modulated by a series  
 488 of peaks/dips centred on  $\theta = 0$ , and a sharp fall-off at larger values of  $|\theta|$ . These features  
 489 are clearly observed in Figure 8(a), which shows the normalised anode response as a function  
 490 of  $\theta$  measured in the laboratory at 3.8 T, for a tube with anode grid orientations  $\phi = 0, 45^\circ$ .  
 491 Both of these features depend on the physical structure (pitch and thickness) of the anode grid  
 492 (Figure 7(b)). Only the plateau is relevant to the operation in CMS, since the ultimate fall-off  
 493 occurs outside of the range of angles encountered in the ECAL endcaps. Also in CMS, the  
 494 rotation angle,  $\phi$ , of the grid was randomised during Dee construction, hence the  $\phi$  effect on  
 495 VPT yield will be averaged out.

496 The dip/peak structure results from secondary electrons drifting in the direction defined by  
 497  $\vec{E} \times \vec{B}$  (perpendicular to the plane of the paper in Figure 7a). An analytical model has been

498 developed from this concept that allows the position of the dips to be predicted [21]. For the  
 499 VPTs operating at 3.8 T, with a difference in anode-dynode potential of 200 V, the first dip is  
 500 predicted to occur at an angle  $\theta_1 = \tan^{-1}(\tan(21.8^\circ)/\cos(\phi))$ . The  $\phi$  dependence results from  
 501 the change in the effective anode grid pitch as a function of the  $\phi$  rotation angle, as shown in  
 502 Figure 7(b). The predicted dip positions for the two angle scans shown in Figure 8(a), which  
 503 are represented by the two arrows, show good agreement with the laboratory data.

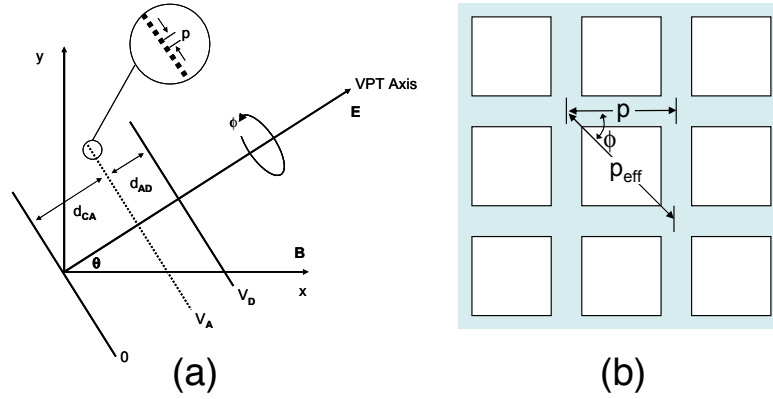


Figure 7: (a): Schematic representation of the electrode structure of a VPT, with the device at an angle  $\theta$  to the magnetic field. The anode grid and dynode are maintained at a potential  $V_A$  and  $V_D$  respectively. (b): Schematic representation of the anode grid, showing how the effective pitch,  $p_{eff}$  varies as the VPT is rotated through an angle  $\phi$  about its axis.

504 In order to obtain the necessary correction factors to transport the pre-calibration constants  
 505 from 0 T to 3.8 T, a series of laser runs were taken in both endcaps at zero and 3.8 T magnetic  
 506 field. The measured dependence of VPT yield as a function of the tilt angle  $\theta$  of the endcap  
 507 VPTs with respect to the magnetic field axis is shown in Figure 8(b). The ratio of VPT yield  
 508 for two laser runs taken at 3.8 T ( $Y_{3.8}$ ) and 0 T ( $Y_0$ ) is plotted, for the angular range of 4 to 18  
 509 degrees. For the endcap VPTs, the majority of tubes (>75%) exhibit tilt angles between 10 and  
 510 18 degrees and the measured value of the ratio  $Y_{3.8}/Y_0$  averaged over all tubes was 88.9%. The  
 511 RMS spread of the data points, indicated by the dashed lines in Figure 8(b), shows the effect of  
 512 averaging over the  $\phi$  angle in CMS.

513 A fit was performed to the measured ratio  $Y_{3.8}/Y_0$  using an empirically-derived function of the  
 514 form:

$$f(\theta) = S \left[ 1 - \frac{x}{2} + \frac{x}{2} \sin \left( \frac{\theta - \theta_0}{\theta_p} \right) \right] \quad (4)$$

515 The parameters  $S$  and  $x$  control the amplitude and vertical offset of the sinusoidal component  
 516 of the function, and  $\theta_0$  and  $\theta_p$  control the horizontal offset and period.

517 Individual correction factors were obtained for all tubes at a given  $\theta$  angle and were used  
 518 to update the existing pre-calibration constants, which were obtained at zero magnetic field.  
 519 Since PN diode readout was not available for these data, the endcap laser amplitudes were  
 520 normalised using the laser amplitude measurements from the barrel supermodules. Since the  
 521 barrel measurements are stable with respect to the magnetic field, such a normalisation sup-  
 522 presses amplitude variations due to the laser light source while preserving the variations of the  
 523 endcap laser amplitude due to the magnetic field.

524 The precision of the measurement was estimated by examining the residuals of the fit to the  
 525 VPT yield ratio  $Y_{3.8}/Y_0$  versus the tilt angle  $\theta$  (Equation 4). In addition, the derived correction  
 526 was applied to the VPT yield at 3.8 T and used to study the stability of the yield with respect to  
 527 the measurements at 0 T for all available data. The estimated precision of this procedure was  
 528 found to be  $\approx 4\%$ , and is mainly due to the averaging over channels with random  $\phi$  angles at  
 529 a constant  $\theta$  value (see the spread of values indicated by the dashed lines in Figure 8(b)).

530 As a result, this measurement should be considered as preliminary. In the future, laser and LED  
 531 data normalised using the PN diode readout will be used to obtain per-channel normalisation  
 532 factors. These will take into account both  $\theta$  and  $\phi$ -dependent effects, and should correct the  
 533 VPT response from existing measurements at 0 T to the CMS operating field of 3.8 T with sub-  
 534 percent precision.

535 This result was also checked over a limited angular range by LED measurements taken at 0 T  
 536 and 3.8 T for a single diffusing sphere (200 channels). The measured ratios  $Y_{3.8}/Y_0$  for LED and  
 537 laser data for these channels agree at the 2% level, which is within the uncertainties quoted  
 538 above for the laser measurements.

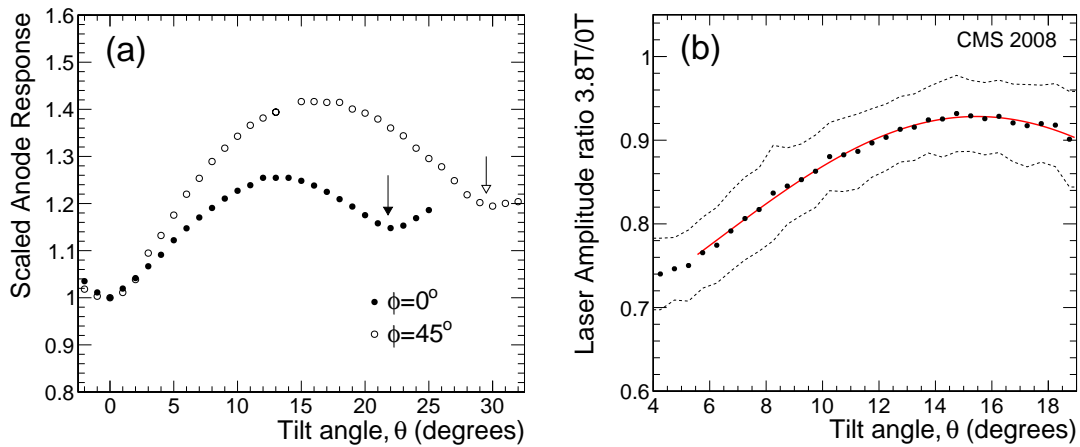


Figure 8: Dependence of VPT yield on angle to magnetic field: (a) Laboratory measurement of the response of a single VPT as a function of tilt angle in a 3.8T axial magnetic field, for two orientation angles,  $\phi$ , of the VPT grid relative to the magnetic field axis. Both sets of data are normalised to unity at the point  $\theta = 0$ ; (b) Normalised ratio of VPT yields  $Y_{3.8}/Y_0$  as a function of tilt angle  $\theta$  for EE laser runs taken in CMS at 3.8 and 0 T magnetic field. The dashed lines represent the RMS spread of the quantity  $Y_{3.8}/Y_0$  for all VPTs at a given  $\theta$  angle. The solid line shows the result of a fit to the data using Equation 4.

## 539 6.2 VPT rate stability

540 Variations in VPT response at zero magnetic field, induced by sudden changes in the illumi-  
 541 nating light pulse rate, have been observed in both the laboratory and in measurements taken  
 542 at the H4 test beam at CERN. Variations in the VPT anode response of 5–20% have been mea-  
 543 sured. This dependence was found to be strongly suppressed in the laboratory at 1.8 T, and  
 544 also suppressed with constant background illumination. An LED pulser system was installed  
 545 in 2008 to provide a constant background rate to each VPT in order to keep them active in the  
 546 absence of LHC collisions and reduce their rate sensitivity.

547 Tests of the VPT rate stability were carried out on 200 VPTs in CMS at 0 T and 3.8 T during late  
 548 2008. The tests were initiated with the VPTs in a quiescent state (no pulsing for the previous 12

549 hours). LED pulsing was turned on delivering an energy equivalent amplitude of 10–15 GeV  
 550 with 10 kHz rate to individual VPTs. This is roughly equivalent to the expected average VPT  
 551 load during LHC running at luminosity of  $10^{33} \text{ cm}^{-2}\text{s}^{-1}$ . The LED light was simultaneously  
 552 monitored by the PN diodes, which were used to provide pulse-to-pulse normalisation of the  
 553 signals measured by the VPTs. LED pulsing continued for 17 hours and was then turned off.  
 554 The response of each VPT was continuously monitored throughout the entire period includ-  
 555 ing several hours prior to and after LED illumination. Figure 9 shows the normalised VPT  
 556 response, averaged over 200 channels, as a function of time during two tests taken at 0 T and  
 557 3.8 T. In both cases, the LED pulsing at high rate was initiated at  $T = -17$  hours, and was  
 558 turned off at  $T = 0$  hours. The variation was measured to be 5% with the CMS magnet at  
 559 0 T. When the test was performed with the CMS magnet at 3.8 T, the average variation of VPT  
 560 response was measured to be less than 0.5%. Further tests on a larger set of VPTs in CMS,  
 561 which will also study the effect on rate sensitivity of exposing the tubes to a constant level of  
 562 background illumination from the LED system (likely at 100 Hz), are planned for 2009.

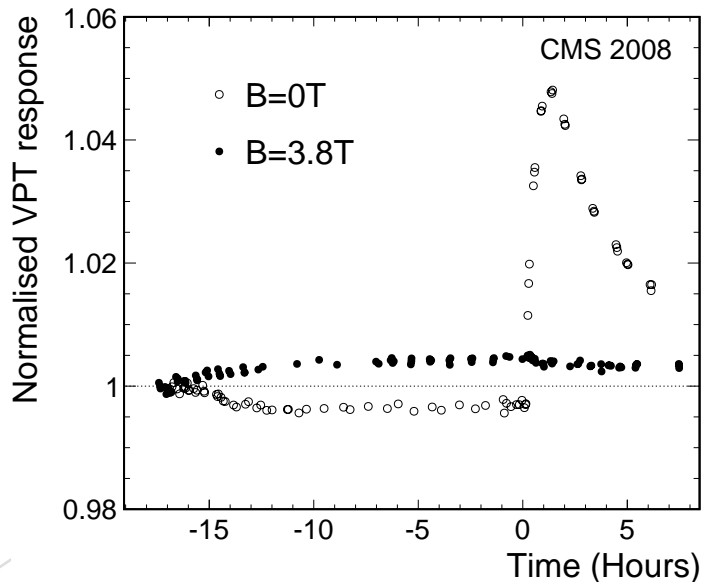


Figure 9: Average normalised response of 200 VPTs for two high rate LED pulsing tests at 0 T (open circles) and 3.8 T (filled circles) during CRAFT. LED pulsing with a rate of 10 kHz was turned on at  $T = -17$  hours and turned off at  $T = 0$  hours. The VPT response was normalised to the value at  $T = -18$  hours in both tests.

## 563 7 Summary

564 The installation of the crystal ECAL in CMS was completed in August 2008 with the insertion  
 565 of the two endcap detectors. The cosmic ray running in October and November 2008 (termed  
 566 CRAFT) represented the first opportunity to operate the entire crystal ECAL for an extended  
 567 period of time, with CMS in its final configuration. Both the Barrel and Endcap detectors op-  
 568 erated stably during this period with greater than 98.5% of channels active. The stability of  
 569 electronics noise, high voltage and temperature during CRAFT are shown to meet the ECAL  
 570 performance targets.

571 The ECAL calibration sequence, which injects laser light, pedestal events and test pulse data  
 572 into the LHC abort gap, was exercised for the first time in CMS during CRAFT. The ultimate

573 purpose of these data is to track changes in crystal transparency under irradiation with an  
574 accuracy of 0.2%. The CRAFT data was used to evaluate the stability of the light monitoring  
575 system in a 200 hour period for 94% of barrel channels and 93% of endcap channels for which  
576 nominal data quality criteria were met. A total of 99.8% of the monitored barrel channels and  
577 98.3% of the monitored endcap channels showed normalised laser amplitude stability of better  
578 than 0.2% (RMS) during this running period.

579 Data taking during CRAFT represented the first opportunity to operate the ECAL endcap de-  
580 tectors in the 3.8 T CMS magnetic field. The 14 648 VPT photodetectors were shown to operate  
581 stably at 3.8 T, and the known dependence of VPT response on the angle of the tube axes to  
582 the magnetic field was measured in situ, and used to update the existing calibration constants  
583 that were obtained at 0 T. The endcap LED system was commissioned during CRAFT, and was  
584 used to measure the dependence of the VPT anode sensitivity to rate, which was better than  
585 0.5% in the high magnetic field of CMS.

586 Finally, cosmic muon events and beam-induced muons in ECAL were used to verify the pre-  
587 calibration constants in the barrel and endcap, which were derived from laboratory and test  
588 beam measurements prior to the installation of the detectors in CMS. These constants, which  
589 will provide initial values for the calibration methods using LHC beam data, and startup LHC  
590 physics, were verified with a precision comparable to the existing measurement uncertainties.  
591 In the barrel, the regional energy scale was verified with a precision of  $\approx 1\%$ . In the endcap,  
592 the precision of the pre-calibration constants at zero magnetic field was improved from 7.4% to  
593 6.3% from the combination of the existing coefficients with those obtained from beam-induced  
594 muons.

## 595 Acknowledgements

596 We thank the technical and administrative staff at CERN and other CMS Institutes, and ac-  
597 knowledge support from: FMSR (Austria); FNRS and FWO (Belgium); CNPq, CAPES, FAPERJ  
598 and FAPESP (Brazil); MES (Bulgaria); CERN; CAS, MST and NSFC (China); MST (Croatia); RPF  
599 (Cyprus); Academy of Sciences and NICPB (Estonia); Academy of Finland, ME and HIP (Fin-  
600 land); CEA and CNRS/IN2P3 (France); BMBF, DFG and HGF (Germany); GSRT and Leventis  
601 Foundation (Greece); OTKA and NKTH (Hungary); DAE and DST (India); IPM (Iran); SFI (Ire-  
602 land); INFN (Italy); KICOS (Korea); CINVESTAV, CONACYT, SEP and UASLP-FAI (Mexico);  
603 PAEC (Pakistan); SCSR (Poland); FCT (Portugal); JINR (Armenia, Belarus, Georgia, Ukraine,  
604 Uzbekistan); MST and MAE (Russia); MSD (Serbia); MCINN and CPAN (Spain); Swiss Fund-  
605 ing Agencies (Switzerland); NSC (Taipei); TUBITAK and TAEK (Turkey); STFC (United King-  
606 dom); DOE and NSF (USA).

## 607 References

- 608 [1] CMS Collaboration, S. Chatrchyan et al., "The CMS experiment at the CERN LHC,"  
609 *JINST* **3** (2008) S08004. doi:10.1088/1748-0221/3/08/S08004.
- 610 [2] M. Raymond et al., "The MGPA Electromagnetic Readout Chip for CMS," in  
611 Proceedings of the 9th Workshop on Electronics for the LHC Experiments, 2003,  
612 CERN-LHCC-2003-055 (2003).
- 613 [3] P. Paganini, "CMS Electromagnetic Trigger commissioning and first operation  
614 experiences," *J. Phys. Conf. Ser.* **160** (2009) 012062.  
615 doi:10.1088/1742-6596/160/1/012062.

- 616 [4] T. Christiansen, "The CMS Magnet Test and Cosmic Challenge," *Nuclear Science*  
617 *Symposium Conference Record, 2006. IEEE* **2** (2006) 906–908.  
618 doi:10.1109/NSSMIC.2006.355993.
- 619 [5] CMS Collaboration, "The CMS Cosmic Run at Four Tesla," *submitted to JINST* (2009).
- 620 [6] CMS Collaboration, "CMS L1 performance paper," *submitted to JINST* (2009).
- 621 [7] CMS Collaboration, "CMS Physics Technical Design Report, Volume II: Physics  
622 Performance." <http://cdsweb.cern.ch/record/942733>. CERN-LHCC-2006-021.
- 623 [8] N. Almeida et al., "The Selective Read-Out Processor for the CMS Electromagnetic  
624 Calorimeter," *IEEE Trans. Nucl. Sci.* **52** (2004) 772–777.  
625 doi:10.1109/TNS.2005.850946.
- 626 [9] P. Adzic et al., "Reconstruction of the signal amplitude of the CMS electromagnetic  
627 calorimeter," *Eur. Phys. J.* **C46S1** (2006) 23–34.  
628 doi:10.1140/epjcd/s2006-02-002-x.
- 629 [10] CMS Collaboration, "Time Reconstruction and Performance of Crystal ECAL," *submitted*  
630 *to JINST* (2009).
- 631 [11] CMS Collaboration, "Measurement of the Muon Stopping Power in PWO," *submitted to*  
632 *JINST* (2009).
- 633 [12] CMS Collaboration, "The Electromagnetic Calorimeter Project: Technical Design  
634 Report." <http://cdsweb.cern.ch/record/349375>. CERN-LHCC-97-033.
- 635 [13] P. Adzic et al., "Energy resolution of the barrel of the CMS electromagnetic calorimeter,"  
636 *JINST* **2** (2007) P04004. doi:10.1088/1748-0221/2/04/P04004.
- 637 [14] D. Renker, "Properties of avalanche photodiodes for applications in high energy physics,  
638 astrophysics and medical imaging," *Nucl. Instrum. Meth.* **A486** (2002) 164–169.  
639 doi:10.1016/S0168-9002(02)00696-4.
- 640 [15] See, for example, the technical reprint from ET Enterprises Ltd., "The determination of  
641 photomultiplier temperature coefficients for gain and spectral sensitivity using the  
642 photon counting technique". <http://www.electrontubes.com/pdf/rp081colour.pdf>.
- 643 [16] See, for example, Figure 29 of the brochure from ET Enterprises Ltd., "Understanding  
644 Photomultipliers".  
645 <http://www.electrontubes.com/Photomultipliers/Understanding.pdf>.
- 646 [17] P. Adzic et al., "Results of the first performance tests of the CMS electromagnetic  
647 calorimeter," *Eur. Phys. J.* **C44S1** (2006) 1–10. doi:10.1140/epjcd/s2005-02-011-3.
- 648 [18] P. Adzic et al., "Intercalibration of the barrel electromagnetic calorimeter of the CMS  
649 experiment at start-up," *JINST* **3** (2008) P10007.  
650 doi:10.1088/1748-0221/3/10/P10007.
- 651 [19] G. Daskalakis, "CMS ECAL calibration strategy," *AIP Conf. Proc.* **867** (2006) 400–407.  
652 doi:10.1063/1.2396978.
- 653 [20] K. W. Bell et al., "Vacuum phototriodes for the CMS electromagnetic calorimeter  
654 endcap," *IEEE Trans. Nucl. Sci.* **51** (2004) 2284–2287. doi:10.1109/TNS.2004.836053.

- 655 [21] R. M. Brown, "The variation in response of the CMS ECAL vacuum phototriodes as a  
656 function of orientation in a strong magnetic field."  
657 [http://cms.cern.ch:80/iCMS/jsp/openfile.jsp?tp=draft&files=584\CMS\\_Note.pdf](http://cms.cern.ch:80/iCMS/jsp/openfile.jsp?tp=draft&files=584\CMS_Note.pdf).  
658 CMS-NOTE 2009/NNNN.

DRAFT